Strain-driven oxygen deficiency in multiferroic $SrMnO_3$ thin films

P. Agrawal,[1,2] J. Guo,[3] P. Yu,[3] C. Hébert,[4] D. Passerone,[2] R. Erni,[1] and M. D. Rossell[1,*]

[1]*Electron Microscopy Center, Empa, Swiss Federal Laboratories for Materials Science and Technology, CH-8600 Dübendorf, Switzerland*

[2]*Nanotech@surfaces laboratory, Empa, Swiss Federal Laboratories for Materials Science and Technology, CH-8600 Dübendorf, Switzerland*

[3]*State Key Laboratory of Low Dimensional Quantum Physics and Department of Physics, Tsinghua University, Beijing 100084, People's Republic of China*

[4]*Interdisciplinary Center for Electron Microscopy (CIME) & LSME - Institut de Physique, École Polytechnique Fédérale de Lausanne, CH-1015 Lausanne, Switzerland*

(Received 23 June 2016; revised manuscript received 16 August 2016; published 1 September 2016)

The structural and electronic properties of a series of $SrMnO_3$ thin films grown on different substrates leading to different biaxial strains are examined by means of aberration-corrected high-angle annular dark-field scanning transmission electron microscopy and electron energy-loss spectroscopy (EELS). Here, we report a comprehensive theoretical investigation on the impact of oxygen nonstoichiometry and strain on the O-K and Mn-$L_{2,3}$ electron energy-loss near-edge structures of $SrMnO_3$ with the aid of the all-electron density functional theory code WIEN2K. Our experimental and theoretical EELS data reveal pronounced peak-height changes and energy shifts as a function of strain, which are ascribed to differences in the oxygen vacancy density rather than to a direct effect of lattice distortions. In addition, we find that the formation of oxygen vacancies in $SrMnO_3$ is likely to be enhanced by tensile strain. Compared to the unstrained material, the vacancy formation energy is reduced by 0.25 eV under 3.78% tensile strain.

DOI: 10.1103/PhysRevB.94.104101

I. INTRODUCTION

In the past decade, there has been a flurry of research activities aimed at discovering new multiferroic materials exhibiting simultaneous magnetic and ferroelectric order with strong magnetoelectric coupling above room temperature. The tremendous interest in this class of multiferroics is motivated by the expectation of integrating them into low-power spintronic nanodevices, where the magnetic order is controlled by low energy consuming electric fields instead of magnetic fields. However, the conventional mechanism for the transition metal cation off-centering in ferroelectrics requires formally empty d orbitals to be available for hybridization with the p orbitals of the surrounding oxygen anions, whereas the formation of magnetic moments usually results from partially filled d shells [1]. This limitation has boosted an intense research on alternative routes to combine ferroelectricity and magnetism in a single phase [2]. In particular, alternative mechanisms for ferroelectricity are most intensively pursued [3]. Thus, in magnetic perovskite-type materials, multiferroism has been achieved by making use of the stereochemical activity of the lone pair electrons of the large A-site cations (like Bi^{3+} and Pb^{2+}), charge ordering, geometrical ferroelectricity, as well as unconventional spin order. Unfortunately, a rather weak ferroic coupling is common to multiferroic materials in which ferroelectricity and magnetic order are associated with two chemically different cations (known as type-I multiferroics). Conversely, the coupling is very strong in materials in which ferroelectricity is magnetically induced (type-II multiferroics), but the polarization in these materials is usually fairly small, typically $\sim 10^{-2}$ $\mu C/cm^2$.

Recently, however, a new route to ferroelectric ferromagnets using strain was proposed by first-principles calculations. Fennie and Rabe [4] predicted that by applying tensile strain to $EuTiO_3$, normally an antiferromagnetic-paraelectric (AFM-PE) material [5], a ferromagnetic-ferroelectric (FM-FE) phase could be produced as a result of a strong interaction between the spin ordering and the lattice phonons, i.e., by the so-called "spin-phonon coupling" [6]. Yet, a very weak magnetoelectric coupling was experimentally confirmed [6]. The origin of the weak ferroic coupling in $EuTiO_3$ was ascribed to magnetism and ferroelectricity originating from different lattice sites [7].

More recently, theoretical calculations suggested that, similarly to $EuTiO_3$, strain-driven multiferroicity associated with spin-phonon coupling should also arise in strained $SrMnO_3$ (SMO) [8]. In bulk form, SMO is observed to have a PE cubic perovskite structure with G-type AFM ordering arising from linear Mn-O-Mn superexchange interactions. Under epitaxial strain a polar instability in the FM phase leads to a substantial energy lowering, which stabilizes the FM-FE multiferroic phase over the bulk AFM-PE phase [8]. But most interesting is the fact that the polar distortion is found to be dominated by the off-centering of the magnetic Mn^{4+} cations from the MnO_6 octahedra along one of the pseudocubic ⟨110⟩ axes [8–10]. Thus the same Mn^{4+} (d^3) cation is responsible to drive both the magnetic and the ferroelectric order. Consequently, a strong magnetoelectric coupling with similar ordering temperatures is foreseen.

However, one aspect that was overlooked in the theoretical predictions is the tendency of the SMO structure to incorporate oxygen vacancies, which makes it very difficult to synthesize fully stoichiometric SMO samples [10,11]. Thus, for example, the large dispersion reported in literature for the Néel temperature of unstrained SMO (between 233 and 260 K) [12–15] is ascribed to differences in the oxygen stoichiometry of the samples used. Similarly, the electronic properties of SMO are largely affected by stoichiometry [15]. Moreover, epitaxial strain is known to critically affect the oxygen vacancy concentration in conventional perovskites.

*marta.rossell@empa.ch

Hence the activation energies of these vacancies can be tuned by tenths of an eV under modest strains of a few percent [16–19]. In particular, for SMO thin films, it was predicted that a small biaxial tensile strain of 2% should increase the oxygen vacancy concentration by one order of magnitude at room temperature [9]. Characterization of the oxygen deficiency of these samples is essential because it might have enormous implications for their potential multiferroic applications as perfectly stoichiometric highly resistive SMO thin films are required [11]. For example, Becher *et al.* [9] suggested that oxygen vacancy order in strained SMO takes place at (100)- or (010)-oriented domain walls, which act as insulating barriers separating different polar domains. On the other hand, Maurel *et al.* [20] speculated that, with increasing tensile strain, accumulation of oxygen vacancies at the SMO/substrate interface frustrate the magnetic interactions and induce a spin-glass effect on the material. Later, Guzmán *et al.* [10] probed by electron energy-loss spectroscopy the oxygen deficiency in a SMO film grown on $(La_{0.3}Sr_{0.7})(Al_{0.65}Ta_{0.35})O_3$ and detected a gradual change in the distribution of oxygen vacancies with an increased population near the substrate interface, where the in-plane tensile strain is largest.

In this work, we have examined the structural and electronic properties of several SMO thin films grown under different strains by using aberration-corrected high-angle annular dark-field scanning transmission electron microscopy (HAADF-STEM) and electron energy-loss spectroscopy (EELS). The experimental EELS results are interpreted with the aid of the all-electron density functional theory (DFT) code WIEN2K. Thus we present a detailed theoretical investigation on the effect of oxygen vacancies on the O-K and Mn-$L_{2,3}$ electron energy-loss near-edge structures (ELNES) of SMO.

II. METHODS

A. Experimental details

The present study was performed on five SMO thin films with thicknesses in the range of 10–13 nm grown by reflection high-energy electron diffraction (RHEED) assisted pulsed laser deposition on $LaSrAlO_4(001)_t$, $LaAlO_3(001)_{pc}$, $(La_{0.3}Sr_{0.7})(Al_{0.65}Ta_{0.35})O_3(001)_{pc}$, $SrTiO_3(001)_c$, and $DsScO_3(110)_o$ substrates, where t, pc, c, and o denote tetragonal, pseudocubic, cubic, and orthorhombic indices, respectively. For simplicity, from now on we will refer to them as LSAO, LAO, LSAT, STO, and DSO. These substrates were used to induce nominal epitaxial strain values of −1.30%, −0.32%, 1.63%, 2.56%, and 3.78%, respectively. In all cases, the SMO films were capped with a DSO layer in order to protect them from deoxidation. All DSO capping layers are crystalline except for the SMO/LAO system, which is protected with an amorphous DSO layer. The SMO films and the DSO capping layers were grown at a substrate temperature of 850 °C using an oxygen pressure of 0.15 mbar. After growth, all films were annealed at 600 mbar of oxygen and 850 °C during 30 min. Subsequently, the samples were cooled down to room temperature at a rate of 10 °C/min. Epitaxial growth was confirmed by x-ray diffraction (XRD) performed on a four-circle Rigaku SmartLab diffractometer with Cu $K\alpha$ radiation [21].

Samples for transmission electron microscopy were prepared in cross section by means of a FEI Helios Nanolab 450S focused ion beam (FIB) instrument. High resolution Z-contrast images were acquired in STEM mode with a HAADF detector using a double spherical aberration-corrected JEOL JEM-ARM200F microscope operated at 200 kV, and equipped with a Gatan Enfinium EELS spectrometer. The annular semidetection range of the annular dark-field detector was calibrated at 90–370 mrad. For the EELS data acquisition, the convergence and collection semiangles were set to 25.3 and 33 mrad, respectively. A dispersion of 0.1 eV per channel was selected in order to cover an energy range of about 200 eV including both the oxygen K and manganese $L_{2,3}$ edges. EELS data were acquired in DualEELS mode in order to have both the low- and core-loss regions. All spectra were deconvoluted using the Fourier-log method to ensure single-scattering distribution, and background subtracted by fitting a decaying power-law function to an energy window just in front of the O and Mn core-loss edge onsets.

The strain in the SMO films was determined by geometric phase analysis (GPA) using the GPA software by HREM Research Inc., which is a plug-in for the image processing package DigitalMicrograph. To minimize errors due to scan instabilities that occur in the slow-scan (y) direction, two HAADF-STEM images rotated by 90° were acquired for each field of view: one with the fast-scan (x) direction aligned along the in-plane (IP) direction, and the second one along the out-of-plane (OOP) direction. For each SMO film, the magnification of the images was calibrated using the substrate lattice spacing aligned parallel to the fast-scan direction. Special care was taken in selecting the SMO reflections in the Fourier transform to avoid artifacts [22]. Thus circular Gaussian masks with a full width at half maximum of $\frac{1}{5}\mathbf{g}_{min}$ (where $\mathbf{g}_{min}$ is the smallest $\mathbf{g}$ vector) were placed around the (101)-type reflections. The GPA software was selected to output strain maps along the IP or OOP directions. The change in strain (measured in %) perpendicular and parallel to the growth axis was determined relative to an internal reference lattice chosen in the substrate area. Subsequently, d spacing maps were obtained by referencing the calculated strain to the substrate spacings.

B. Computational details

The electronic structure of $SrMnO_3$ grown on different substrates was calculated by the full-potential linearized augmented plane-wave [23] (FP-LAPW) method within the density functional theory as implemented in the WIEN2K package [24]. First-principles calculations were performed using the generalized gradient approximation GGA+U method [25]. The Perdew-Burke-Ernzerhof (PBE) generalized gradient approximation (GGA) was employed for the exchange-correlation function. A Coulomb interaction $U = 2.7$ eV and on-site exchange interaction $J_H = 1.0$ eV were used to treat the Mn d electrons [8]. The same U values were adopted to perform all calculations with WIEN2K. All calculations were carried out using $2 \times 2 \times 2$ or $2 \times 2 \times 1$ supercell structural models based on an orthorhombic unit cell [8] composed of five atoms, unless otherwise stated (see below for details). A shifted $4 \times 4 \times 4$ special k-point mesh with a modified

tetrahedron integration scheme [26] for the sampling of the Brillouin zone was employed. Convergence was tested on bulk SMO using k-mesh distributions of $4 \times 4 \times 4$, $6 \times 6 \times 6$, and $10 \times 10 \times 10$, which showed that the $4 \times 4 \times 4$ sampling was sufficient for the present system. The valence and core states were separated by 6.5 Ry of energy and the plane-wave cutoff parameter $R_{\mathrm{mt}} \times k_{\mathrm{max}}$ was set to 7.00. The EELS spectra were computed using the TELNES 3.0 module [27,28] of WIEN2K using an electron beam energy of 200 kV, semicollection angle of 5 mrad, and semiconvergence angle of 2 mrad. A broadening of 1.0 eV was used to account for the instrumental energy resolution. The module allows one to compute spectra with and without removal of a core-hole electron (see below).

III. RESULTS AND DISCUSSION

A. Quantification of the epitaxial strain from HAADF-STEM images

HAADF-STEM images of all five SMO films are shown in Fig. 1. High-quality single-crystalline epitaxial thin films with atomically sharp film/substrate interfaces were obtained in all cases. Representative lattice parameter maps showing the variation in lattice parameter along the OOP and IP directions are shown in the central and right panels of Fig. 1, respectively. Overall, the IP parameters of the SMO films and the substrate materials show negligible differences indicating that the SMO films are fully strained. Although, misfit dislocations are occasionally observed at the top SMO/DSO interface [see, e.g., Figs. 1(c) and 1(d)]. Besides, the OOP parameters are homogeneously strained over the whole thickness of the thin films. Thus no strain gradients from the substrate interface towards the upper layers of the films were detected, as reported in Ref. [10]. Subsequently, the IP and OOP lattice parameters for each film were determined from each image by averaging over a rectangular area containing the whole SMO film. The obtained values as well as the c/a ratio (where c/a is the ratio between the OOP and IP pseudocubic lattice), and the unit-cell volume are plotted against the epitaxial strain in Fig. 2. One can see that the first two quantities change linearly as a function of the imposed strain between -1.30% and 2.56%, that is, excluding the SMO/DSO film. Nevertheless, it is found that the IP lattice parameters of the SMO films grown on LSAT, STO, and DSO are larger than the OOP parameters, while this is reversed for the SMO films grown on LSAO and LAO. The maximum tetragonality, measured by GPA, is achieved for the compressed SMO/LSAO thin film, where $c/a = 1.045$, $a = 3.76$ Å, and $c = 3.93$ Å. However, from purely geometrical considerations, one would expect the c/a ratio to be largest for the SMO/DSO film. The presence of occasional cracks in the SMO/DSO film helps to explain the partial stress relief in this film. Figure 3 shows a cross-section view of a typical crack in the SMO film grown on DSO. Indeed, cracks were previously observed in SMO films grown on LSAT substrates [9], and we believe they are most likely formed due to stress relaxation during the TEM specimen preparation, i.e., when the FIB lamellae are thinned below 100 nm. This assumption is based on x-ray diffraction measurements showing that the SMO thin film grows coherently on DSO with an OOP parameter of 3.76 Å [21], distinctly shorter than the one extracted

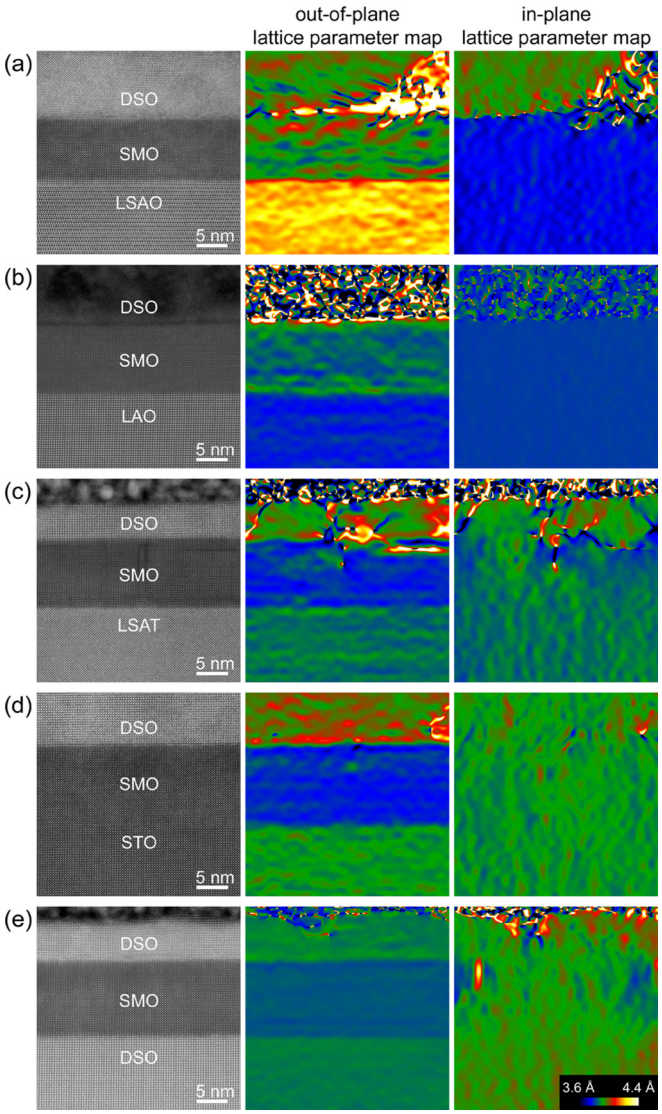

FIG. 1. Strain analysis of SMO films grown on (a) LSAO, (b) LAO, (c) LSAT, (d) STO, and (e) DSO. Maps of out-of-plane (middle panels) and in-plane (right panels) lattice parameters determined from GPA of HAADF-STEM images (left panels). The color scale is the same for all panels.

by GPA of the atomic-resolution HAADF-STEM images. Moreover, additional evidence is obtained by inspecting the HAADF-STEM images of the cracks; see Fig. 3. It is apparent that no crack propagation takes place into the DSO capping layer, meaning that the capping layer was deposited on a perfectly coherent and uncracked SMO/DSO film.

Interestingly, in all films, the volume of the SMO unit cell is larger than the bulk cubic SMO structure ($a = 3.80$ Å and $V = 54.87$ Å^3) [12]. Besides, the unit-cell volume is not preserved but expands under increasing tensile strain. In order to evaluate whether the monotonic volume increase with tensile strain can be simply understood through a Poisson-type expansion we evaluated the Poisson coefficient of the films. The Poisson's ratio can be calculated from $\nu = 1/(1 - 2\varepsilon_{xx}/\varepsilon_{zz})$, where ε_{xx} and ε_{zz} are the in-plane and out-of-plane lattice strains, respectively [29,30]. For our system we estimated a $\varepsilon_{xx}/\varepsilon_{zz}$

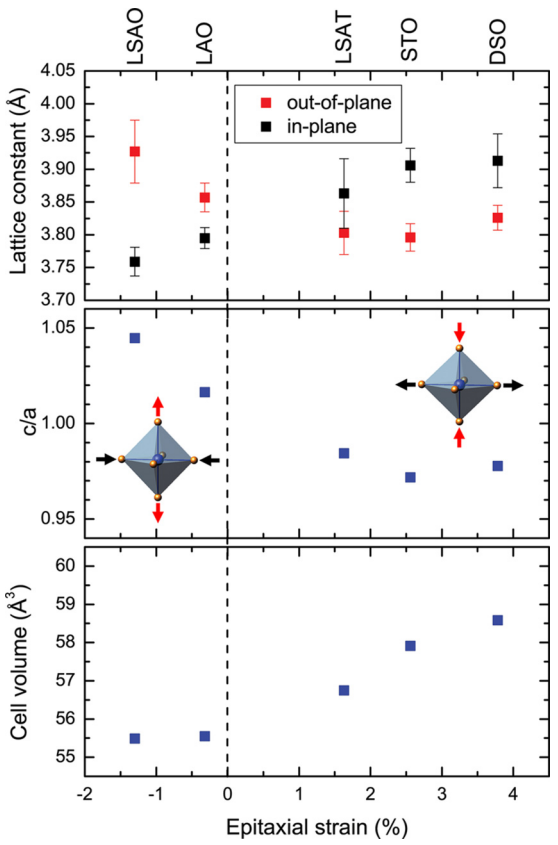

FIG. 2. Structural parameters obtained by GPA of HAADF-STEM images as function of nominal strain. (a) Out-of-plane and in-plane lattice parameters of the SMO pseudocubic unit cell; (b) c/a lattice parameter ratio; (c) unit-cell volume. Insets: schematic illustrations of the epitaxial strain accommodation assuming bond-length changes only.

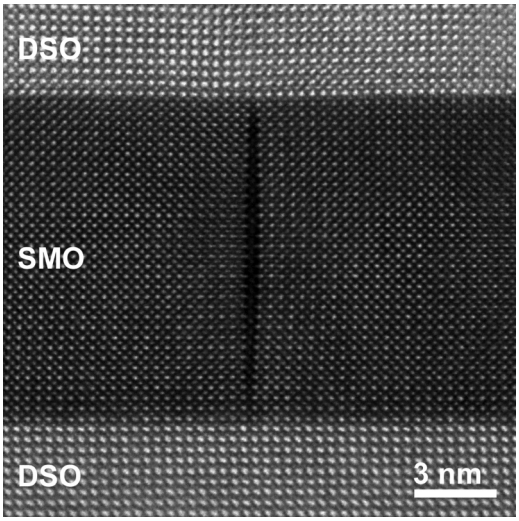

FIG. 3. HAADF-STEM image of the DSO/SMO/DSO film showing the presence of a crack. Note that the crack does not propagate into the top DSO capping layer.

ratio of -1.59, from which a Poisson's ratio $\nu = 0.24$ is obtained. This value is noticeably smaller than the ν values associated to perovskite manganites, typically between 0.35 and 0.41 [30–32] (note that the unit cell volume is preserved only for $\nu = 0.5$). Thus the large lattice expansion associated with biaxial tensile strain is most likely due to an increase of the oxygen vacancy concentration as the film deviates from the stoichiometric $\delta = 0$ in $SrMnO_{3-\delta}$. This prediction is in good agreement with previous calculations showing that the $CaMnO_3$ structure can accommodate in-plane tensile strain by increasing its concentration of oxygen vacancies [17].

B. EEL spectroscopy studies

To confirm that the observed volume increase with increasing tensile strain is coupled to the oxygen-vacancy formation, EELS data were acquired for all the samples. Figure 4 shows a comparison of the manganese $L_{2,3}$ and oxygen K edges among the series of SMO films. Clearly, the obtained spectra show pronounced peak-height changes and energy shifts as a function of strain.

The Mn-$L_{2,3}$ edge corresponds to excitations of the Mn $2p$ electrons into empty Mn $3d$ states. These transitions produce two main characteristic features, or white lines, due to the spin-orbit splitting of the Mn $2p$ core hole into $2p_{3/2}$ and $2p_{1/2}$ states. They are indicated as L_3 and L_2 in Fig. 4(a), respectively. To facilitate visual comparison of the data, all spectra were normalized to the intensity maxima of the L_3 edge and an energy shift of a few eV was applied to align the L_2 edges. Clearly, the L_3 peaks corresponding to the SMO films under tensile strain appear at a lower energy ($\sim$1.4 eV) than those corresponding to the compressed SMO films. Additionally, the relative intensity of the L_2 line with respect to the L_3 line progressively decreases from LSAO (black curve) to DSO (red curve). Both these observations, the increase in the spin-orbit splitting and of the L_3/L_2 ratio, indicate an increase of the electron doping of the Mn $3d$ e_g band with tensile strain.

Complementary information can be obtained from the O-K edge, resulting from excitations of O $1s$ electrons into available O $2p$ empty states. The O-K near-edge structure of the SMO strained series in Fig. 4(b) exhibits three major peaks, a, b, and c, caused by hybridizations of unoccupied O $2p$ orbitals with Mn $3d$, Sr $4d$, and Mn $4sp$ orbitals, respectively [33–35]. For clarity, all spectra were normalized to the intensity maxima of the main peak b, and the same energy shift used to align the Mn-L_2 edges was applied to the O-K spectra. By doing so, the O-K_b peak in all spectra is aligned at 537 eV, while the positions and intensity of the adjacent O-K_a and O-K_c peaks change steadily with strain as indicated with dashed lines. According to previous reports, since the O-K_a prepeak has a very strong contribution from the Mn $3d$ e_g band occupancy, it can be used to extract information on the Mn oxidation state [36,37].

Several approaches can be employed to quantitatively determine the Mn oxidation state from the energy-loss near-edge structures (ELNES) of the O-K and Mn-$L_{2,3}$ edges. Specifically, changes in the Mn-$L_{2,3}$ white-line intensity ratio, the Mn-L_3 linewidth, the normalized O-K_a intensity, and the energy separation between the O-K_a and O-K_b edges, the

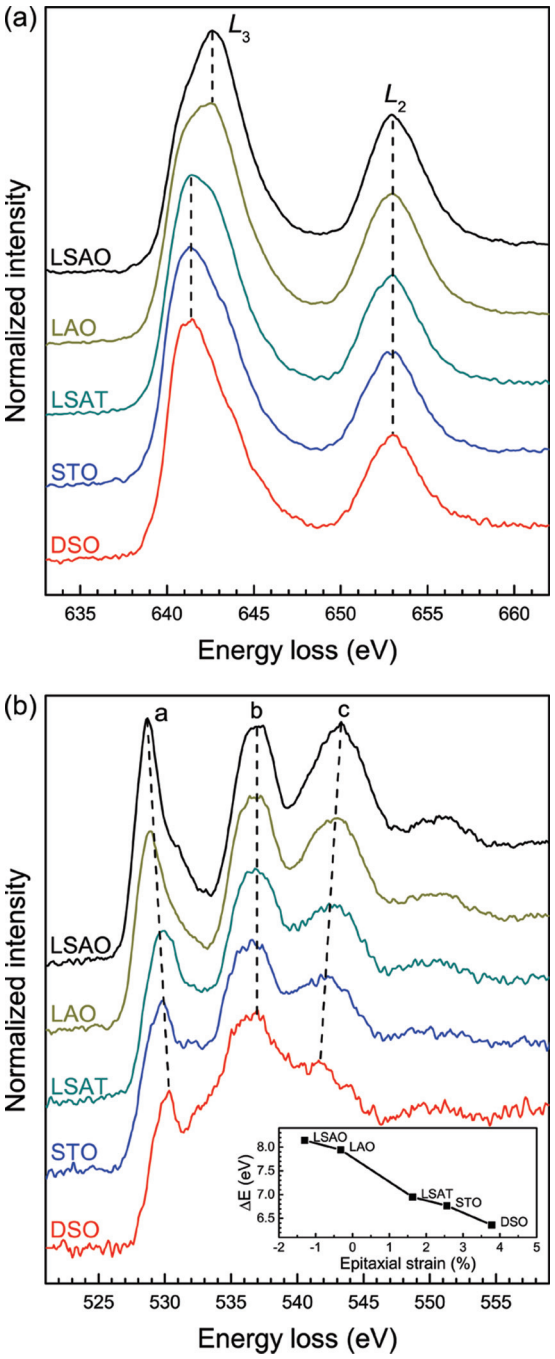

FIG. 4. Comparison of Mn-L and O-K edges among the SMO films grown on different substrates. (a) The energy scales have been shifted so the L_2 lines match. The intensity is normalized to the L_3 line. Dashed lines are used to show the shift in energy of the L_3 peak. (b) The energy scales have been shifted so the main peaks at 537 eV are aligned, and the intensity normalized. Dashed lines are used to show the shift in energy of the adjacent peaks. The energy difference between the oxygen O-K_b main peak and the O-K_a prepeak is quantitatively shown in the inset. All spectra are displaced vertically for clarity.

Mn-L_3 and Mn-L_2 edges, and the O-K_a and Mn-L_3 edges have been thoroughly addressed [36–39]. Nevertheless, the determination of the energy difference between the oxygen O-K_b main peak and the O-K_a prepeak appears to be the most accurate method and less dependent on spectral noise [36,38], and has been successfully applied to $SrMnO_3$ thin films [9,17]. Here, we estimated the local oxidation state of the SMO films by applying this procedure as reported by Varela *et al.* [36]. Thus, by fitting Gaussian peaks to the O-K_a and O-K_b peaks, the peak positions were determined and the energy difference [see inset in Fig. 4(b)] was used to obtain an average oxidation state of +4.04, + 3.98, + 3.70, + 3.65, and +3.53 for the SMO films grown on LSAO, LAO, LSAT, STO, and DSO, respectively. Clearly, the increment in the tensile strain leads to a reduction in the manganese oxidation state.

C. Interpretation of the EEL spectra

We compared our experimental spectra with theoretical ELNES to get a better insight into the effect of oxygen vacancies on the O-K and Mn-$L_{2,3}$ edge fine structures. For this purpose, three systems out of five were selected for the EELS calculations, namely LSAO, LSAT, and DSO. They correspond to the maximum compression (LSAO) and tensile (DSO) strains, and an additional intermediate point (LSAT) in the tensile regime.

The epitaxial constraint was set by fixing the IP parameters to match those of the experimental substrates. Thus the OOP lattice parameters and internal atomic coordinates were optimized for all the structures. The experimental substrate parameters, and the measured and optimized OOP parameters, are tabulated in Table I. Note that for LSAO the optimized c parameter is in very good agreement with the experimental value, while for the films under tensile strain (LSAT, DSO) the optimized parameters are about 5% smaller than the experimental ones, suggesting the presence of oxygen vacancies in the experimental tensile-strained SMO films.

To clarify the influence of strain and oxygen vacancies on the electronic structure of SMO, each effect was addressed separately. Three sets of calculations were performed: one with strained SMO structures without oxygen vacancies, another with unstrained SMO structures containing oxygen vacancies, and a last one with strained SMO structures containing oxygen vacancies.

Strained + no vacancies. For all three structures, a 2×2×2 supercell and optimized lattice parameters were used in the calculations.

Unstrained + vacancies. For this set of calculations all supercell structural models were based on a cubic unit cell with lattice parameter $c = 3.80$ Å [12]. A 2 × 2 × 2 supercell was modeled for LSAT by removing one oxygen out of $Sr_8Mn_8O_{24}$, and a 2 × 2 × 1 supercell was used for DSO by removing one oxygen out of $Sr_4Mn_4O_{12}$ to get a Mn oxidation state of +3.75 and +3.50, respectively. These values are very close to the

TABLE I. Experimental lattice parameters and optimized out-of-plane parameters calculated for strained SMO structures without oxygen vacancies.

Substrate	a=b (Å)	c (Å)	Optimized c parameter (Å)
LSAO	3.756	3.927	3.935
LSAT	3.868	3.803	3.624
DSO	3.955	3.826	3.626

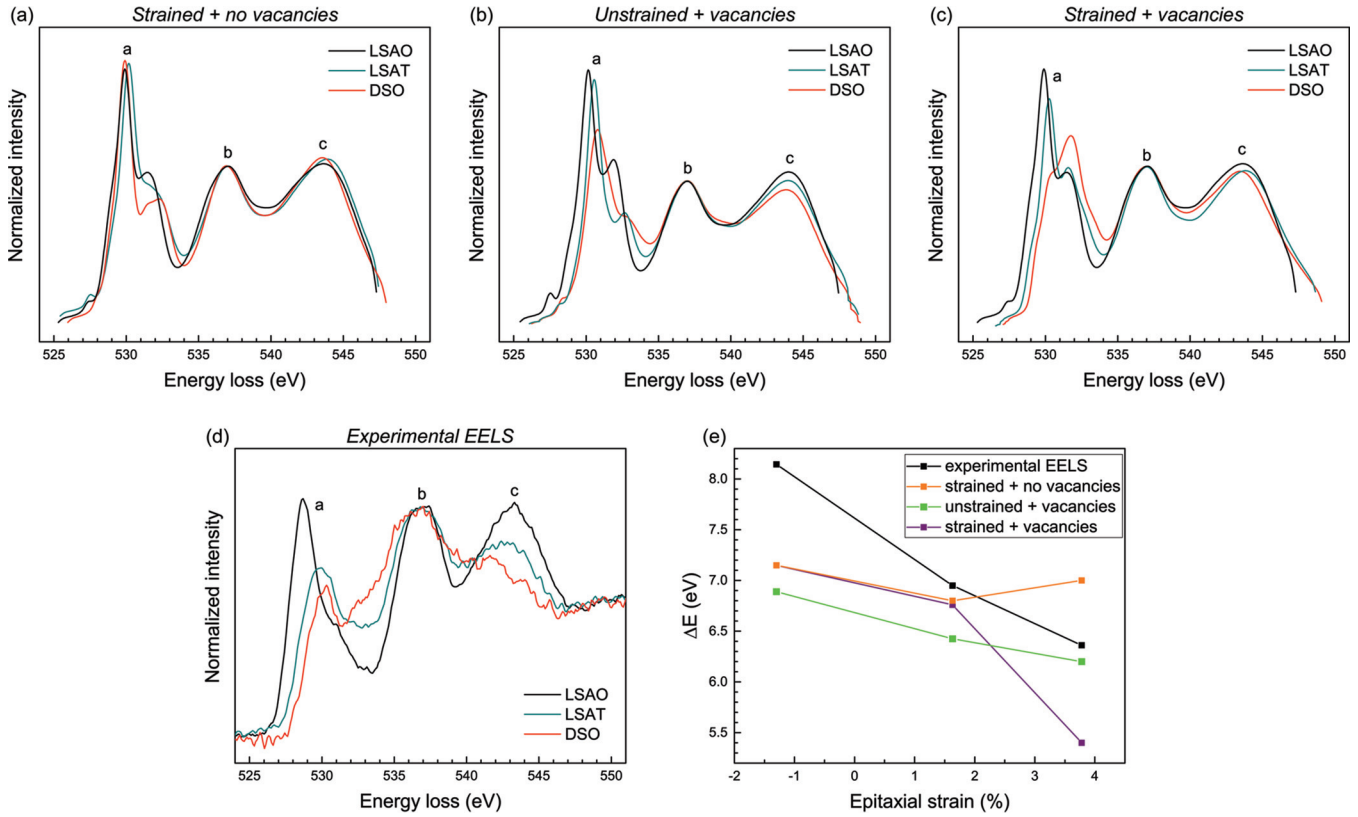

FIG. 5. O-K edge EEL spectra of SMO structures on LSAO, LSAT, and DSO. (a) The O-K edge spectra are calculated assuming strained lattice parameters and no oxygen vacancies. (b) The O-K edge spectra are calculated assuming unstrained lattice parameters and the presence of oxygen vacancies. (c) The O-K edge spectra are calculated assuming strained lattice parameters and the presence of oxygen vacancies. (d) Experimental O-K edge spectra. (e) Energy difference between the O-K_a prepeak and the O-K_b main peak as a function of epitaxial strain for all four cases.

ones observed experimentally, i.e., Mn(LSAT) $= +3.70$ and Mn(DSO) $= +3.53$. Subsequently, the lattice parameters of the cells were kept unaltered and the internal atomic coordinates were optimized.

Strained + vacancies. A $2 \times 2 \times 2$ supercell (based on an orthorhombic cubic unit cell) was modeled for LSAT by removing one oxygen out of $Sr_8Mn_8O_{24}$, and a $2 \times 2 \times 1$ supercell was used for DSO by removing one oxygen out of $Sr_4Mn_4O_{12}$. The optimized lattice parameters were used for the calculations, and then the internal atomic positions were relaxed.

The O-K edge EELS spectra were calculated for all three cases. Matrix elements of the dipole operator were computed between the 1s state of the excited oxygen and the unoccupied states. The calculations were repeated for all nonequivalent oxygen atoms and appropriately averaged. For the fully stoichiometric strained SMO structure on LSAO, we performed calculations introducing half a core hole (i.e., the core level half occupied with an electron in the excited state), and assuming the core hole to be completely screened in order to assess the validity of the two methods. In the limit of large supercell sizes, with the holes sufficiently diluted, calculations done with half a core hole should reproduce the experiment more faithfully and the screening should come out as a result of the electronic structure relaxation induced by the core hole. Taking half a core hole is called the Slater's transition potential approach [40,41] and is shown to include relaxation effects to the second order. We compared calculations using a larger supercell and half a core hole with a corresponding smaller one with no core hole, and we found that both approximations are in very good agreement with the experiment, although the details of the peaks in the calculated ELNES fit slightly better with the experiment when running calculations using a partial core hole. Nevertheless, due to the good match between the two approaches and in order to reduce computation time, we performed the complete set of calculations without core hole.

The calculated oxygen K edge spectra of the strained and unstrained SMO structures with and without oxygen vacancies are shown in Fig. 5. Similar to the experimental data, all obtained spectra are normalized to the intensity maxima of the O-K_b peak, and an energy shift of a few eV was applied to align the peak at 537 eV. The calculated O-K edge spectra assuming the presence of oxygen vacancies [Figs. 5(b) and 5(c)] compare very well with the experimentally obtained O-K edge spectra [Fig. 5(d)]. The good agreement concerns the trend in energy difference between the O-K_a prepeak and the O-K_b main peak, as well as the intensity ratio between the two peaks which decreases with increasing tensile strain. On the other hand, if no vacancies are included in the structural models, neither the experimentally observed depletion of the O-K_a peak with respect to the O-K_b peak nor the peak energy difference decrease upon increasing tensile strain is

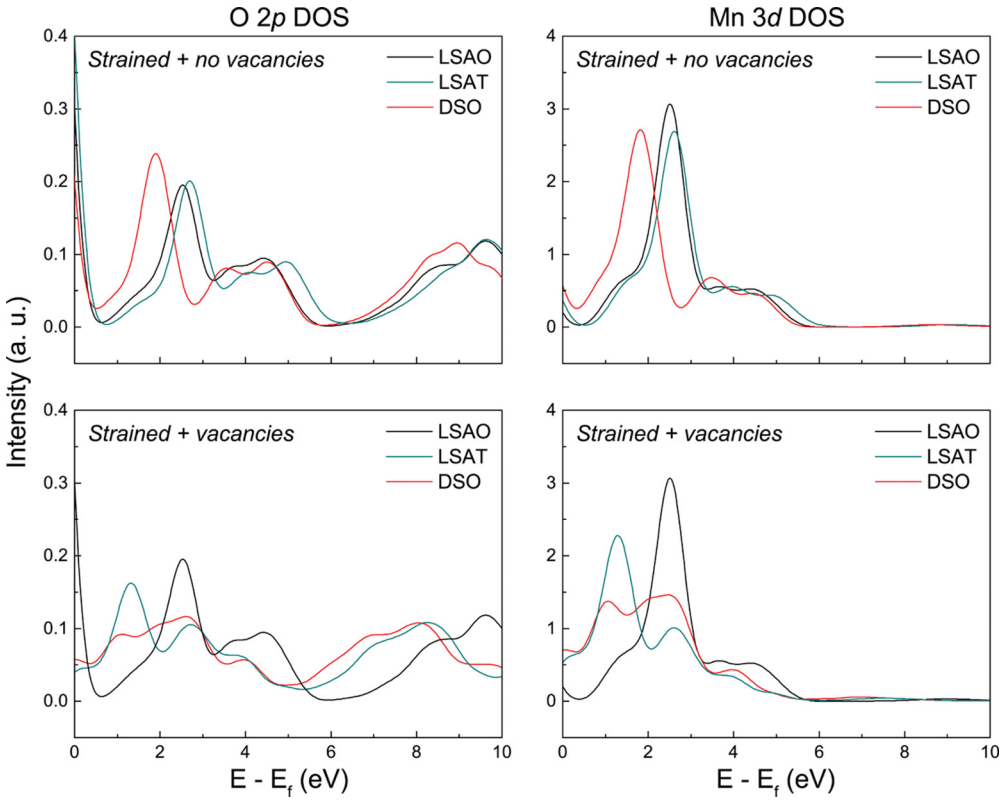

FIG. 6. Projected electron density of the Mn 3*d* and O 2*p* states in *strained* SMO structures on different substrates (LSAO, LSAT, and DSO) with and without oxygen vacancies.

reproduced [Fig. 5(a)]. These findings are summarized in Fig. 5(e), which shows the energy difference between the O-K_a and O-K_b peaks for all different cases. Note that the calculations show underestimated values compared to the experimental results. This is because calculations were performed without the inclusion of the core-hole corrections; when running the calculations using a partial core hole we observed a better agreement with the EELS data. Nevertheless, the theoretical calculations shown here reproduce well the trend in the experimental data. The simulations assuming the presence of oxygen vacancies in the strained SMO structures give the best match to the experimental results, whereas for the strained SMO structures without oxygen vacancies the energy difference is almost constant across the different substrates. Besides, we find that the SMO structures that incorporate oxygen vacancies are energetically more favorable in the presence of tensile strain (by 0.29 eV for LSAT and 0.30 eV for DSO). The origin of this energy reduction is mainly electrostatic, as tensile strain reduces the electron-electron repulsion along the broken Mn-O-Mn bond axis (see below) [17].

Shown in Fig. 6 is the projected electron density of states (pDOS) of the O 2*p* and Mn 3*d* states in the *strained* SMO structures on LSAO, LSAT, and DSO with and without oxygen vacancies. We notice the following

(1) One sharp peak around 2 eV is observed in the pDOS for both O 2*p* and Mn 3*d* for all SMO structures *without vacancies* (see top panels in Fig. 6).

(2) When comparing the pDOS for the structures *with vacancies*, it is evident that the O 2*p* and Mn 3*d* peaks at ∼2 eV markedly vary in the three models; they are split in two components for the SMO structures on LSAT and DSO, and are shifted to lower energies (bottom panels in Fig. 6).

(3) The O 2*p* peaks at ∼9 eV are further shifted toward the Fermi level in the SMO structures *with vacancies*.

Additionally, to provide a basis for the interpretation of the EELS spectra, we decomposed the total pDOS of the O 2*p* states into contributions originating from different oxygen atoms. Thus we separated the contributions arising from the oxygen atoms surrounding the Mn ion sitting next to the

TABLE II. Calculated Mn–O interatomic distances in SMO on LSAO, LSAT, and DSO.

	Mn–O distances (Å)					
	Without vacancy					
Substrate	O1	O2	O3	O4	O5	O6
LSAO	1.88	1.88	1.88	1.88	1.97	1.97
LSAT	1.93	1.93	1.93	1.93	1.81	1.81
DSO	1.98	1.98	1.98	1.98	1.81	1.81
	With vacancy					
Substrate	O1	O2	O3	O4	O5	O6
LSAT						
Close	1.92	1.92	1.80		1.80	1.80
Far	1.97	1.97	1.91	1.95	1.81	1.81
DSO						
Close	1.96	1.96	1.80		1.85	1.85
Far	2.02	2.02	1.99	1.97	1.81	1.81

oxygen vacancy from those far away from the oxygen vacancy. These oxygen atoms are henceforth denoted as *close* and *far*, respectively. The Mn–O interatomic distances for all oxygen atoms are tabulated in Table II. In both LSAT and DSO cases, the results show that the formation of oxygen vacancies results in a decrease in the average Mn–O_{close} interatomic distances. To see the effect of these two different sets of oxygen atoms (*close* and *far*) on the EELS spectra, the calculated EELS spectra are plotted together with the corresponding decomposed O $2p$ states in Fig. 7. In the left panel, we show the results for the less strained SMO structure on LSAT, where 8 O *close* and 15 O *far* atoms are present. Focusing on the peak at ∼2 eV, we note that the DOS of the O $2p$ states arising from the O *close* atoms are peaked at a higher energy. However, the largest contribution to the O $2p$ states arises from the O *far* atoms and is found at lower energies. The EELS spectrum reflects the relative concentration of O *far* and O *close* atoms. On the other hand, for the more strained SMO structure on DSO with a larger density of oxygen vacancies (see right panel of Fig. 7), 7 O *close* and 4 O *far* atoms are present. Also in this case the splitting at ∼2 eV is evident, but the largest peak is found at higher energies due to the increased concentration of O *close* atoms. This results in a shift of the O-K_a EELS peak to higher energies. Overall, the net effect in the O-K EELS spectra is that the distance between the O-K_a and O-K_b peaks is reduced due to the presence of vacancies in the SMO structure, in agreement with the experimental EELS data [see Fig. 5(d)].

Lastly, the vacancy formation energy was also calculated based on the study from Aschauer *et al.* [17]. We compared the total energies of the stoichiometric $SrMnO_3$ unit cell and the strained supercells containing oxygen vacancies. The oxygen vacancy formation energy is tabulated in Table III for both SMO structures on LSAT and DSO under tensile strain. Compared to the unstrained material, the formation energy of the oxygen vacancies is reduced by 0.25 eV under 3.78% tensile strain. Thus we conclude that tensile strain favors the formation of oxygen vacancies.

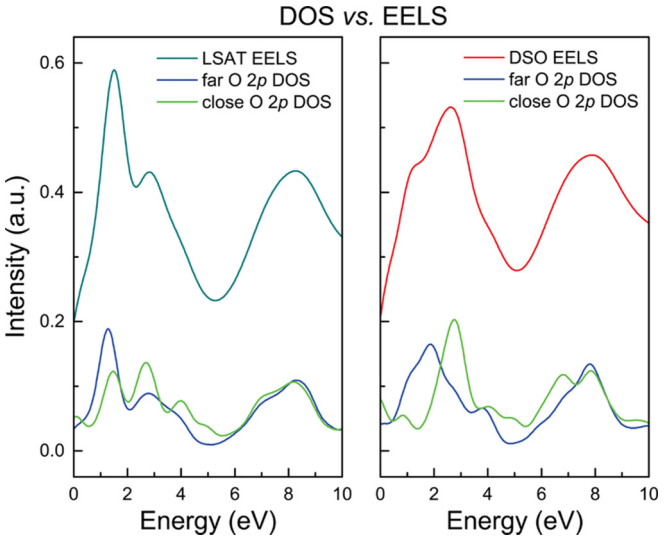

FIG. 7. Comparison of the calculated O-K edge EEL spectra with corresponding DOS of the O $2p$ states decomposed into contributions from the *close* and *far* oxygen atoms for SMO on LSAT (left) and on DSO (right).

TABLE III. Oxygen vacancy formation energy in strained SMO structures on LSAT and DSO substrates.

Substrate	Strain (%)	$\triangle E_{form}$ (eV)
LSAT	1.63	−0.08
DSO	3.78	−0.25

IV. CONCLUSIONS

In the present work, we have thoroughly investigated the structural and electronic properties of epitaxial SMO films deposited on different substrates leading to different strains. In particular, we have examined how the oxygen vacancy density is modified by biaxial strain by means of aberration-corrected HAADF-STEM and EELS. Our experimental EELS data reveal pronounced peak-height changes and energy shifts as a function of strain, which were previously ascribed to differences in the oxygen vacancy density [9,10,36]. Thus our results suggest that the observed energy difference decrease between the O-K_a prepeak and the O-K_b main peak with increasing tensile strain is concomitant with an increase of oxygen vacancies. The formation of oxygen vacancies is charge compensated by reducing the formal oxidation state of the Mn cations, as inferred from the changes observed in the Mn-$L_{2,3}$ edges.

The experimental findings are complemented with all-electron density functional theory based WIEN2K calculations of the density of electron states and of the electron energy-loss near-edge structure. For this, systematic simulations with different oxygen vacancy concentrations and strains are compared with the EELS experimental results. We show that the O-K and Mn-$L_{2,3}$ electron energy-loss near-edge structures are strongly modified by oxygen nonstoichiometry and, to a lesser extent, by strain (only when combined with the presence of oxygen vacancies). Remarkably, our calculations also show that strain solely does not change the intensity nor the distance between the O-K_a and O-K_b peaks. By decomposing the total projected electron density of states of the O $2p$ states into contributions originating from different oxygen atoms we observe that the DOS of the O $2p$ states arising from the oxygen atoms sitting close to the oxygen vacancies are peaked at a higher energy than those far away from the vacancies. The net effect in the O-K EELS spectra is that the distance between the O-K_a and O-K_b peaks is reduced due to the presence of vacancies in the SMO structure. Thus the results presented clarify the origin of the peak-height changes and energy shifts of the O-K and Mn-$L_{2,3}$ edge-fine structures in SMO.

Additionally, we show that compared to the unstrained material the formation energy of oxygen vacancies is reduced by 0.25 eV under 3.78% tensile strain. It thus follows that the formation of oxygen vacancies in the $SrMnO_3$ structure is likely to be enhanced by tensile strain. However, no tensile-strain-induced oxygen vacancy ordering was observed for our SMO films, as suggested by Becher *et al.* [9].

Finally, we anticipate that the presence of oxygen vacancies might hinder the potential multiferroic applications of SMO as highly resistive thin films are required.

ACKNOWLEDGMENTS

This research was supported by the Swiss National Science Foundation under Project No. 200021_147105. The research at Tsinghua was financially supported by the National Natural Science Foundation of China (Grant No. 11274194) and the National Basic Research Program of China (Grant No. 2015CB921700). Access to the TEM facilities at IBM Research-Zurich, Switzerland, under the IBM/Empa Master Joint Development Agreement is gratefully acknowledged.

[1] N. A. Hill, J. Phys. Chem. B **104**, 6694 (2000).
[2] D. A. Khomskii, Physics **2**, 20 (2009).
[3] R. Ramesh and N. A. Spaldin, Nat. Mater. **6**, 21 (2007).
[4] C. J. Fennie and K. M. Rabe, Phys. Rev. Lett. **97**, 267602 (2006).
[5] T. Katsufuji and H. Takagi, Phys. Rev. B **64**, 054415 (2001).
[6] J. H. Lee, L. Fang, E. Vlahos, X. Ke, Y. W. Jung, L. Fitting Kourkoutis, J.-W. Kim, P. J. Ryan, T. Heeg, M. Roeckerath, V. Goian, M. Bernhagen, R. Uecker, P. C. Hammel, K. M. Rabe, S. Kamba, J. Schubert, J. W. Freeland, D. A. Muller, C. J. Fennie, P. Schiffer, V. Gopalan, E. Johnston-Halperin, and D. G. Schlom, Nature (London) **466**, 954 (2010).
[7] T. Birol, N. A. Benedek, H. Das, A. L. Wysocki, A. T. Mulder, B. M. Abbett, E. H. Smith, S. Ghosh, and C. J. Fennie, Curr. Opin. Solid State Mater. Sci. **16**, 227 (2012).
[8] J. H. Lee and K. M. Rabe, Phys. Rev. Lett. **104**, 207204 (2010).
[9] C. Becher, L. Maurel, U. Aschauer, M. Lilienblum, C. Magén, D. Meier, E. Langenberg, M. Trassin, J. Blasco, I. P. Krug, P. A. Algarabel, N. A. Spaldin, J. A. Pardo, and M. Fiebig, Nat. Nanotechnol. **10**, 661 (2015).
[10] R. Guzmán, L. Maurel, E. Langenberg, A. R. Lupini, P. A. Algarabel, J. A. Pardo, and C. Magén, Nano Lett. **16**, 2221 (2016).
[11] S. Kamba, V. Goian, V. Skoromets, J. Hejtmánek, V. Bovtun, M. Kempa, F. Borodavka, P. Vaněk, A. A. Belik, J. H. Lee, O. Pacherová, and K. M. Rabe, Phys. Rev. B **89**, 064308 (2014).
[12] T. Takeda and S. Ohara, J. Phys. Soc. Jpn. **37**, 275 (1974).
[13] K. Kikuchi, H. Chiba, M. Kikuchi, and Y. Syono, J. Solid State Chem. **146**, 1 (1999).
[14] O. Chmaissem, B. Dabrowski, S. Kolesnik, J. Mais, D. E. Brown, R. Kruk, P. Prior, B. Pyles, and J. D. Jorgensen, Phys. Rev. B **64**, 134412 (2001).
[15] R. Søndenå, P. Ravindran, S. Stølen, T. Grande, and M. Hanfland, Phys. Rev. B **74**, 144102 (2006).
[16] A. Kushima, S. Yip, and B. Yildiz, Phys. Rev. B **82**, 115435 (2010).
[17] U. Aschauer, R. Pfenninger, S. M. Selbach, T. Grande, and N. A. Spaldin, Phys. Rev. B **88**, 054111 (2013).
[18] L.-Y. Gan, S. O. Akande, and U. Schwingenschlögl, J. Mater. Chem. A **2**, 19733 (2014).
[19] J. R. Petrie, C. Mitra, H. Jeen, W. S. Choi, T. L. Meyer, F. A. Reboredo, J. W. Freeland, G. Eres, and H. N. Lee, Adv. Funct. Mater. **26**, 1564 (2016).
[20] L. Maurel, N. Marcano, T. Prokscha, E. Langenberg, J. Blasco, R. Guzmán, A. Suter, C. Magén, L. Morellón, M. R. Ibarra, J. A. Pardo, and P. A. Algarabel, Phys. Rev. B **92**, 024419 (2015).
[21] J. Guo *et al.* (unpublished).
[22] J. J. P. Peters, R. Beanland, M. Alexe, J. W. Cockburn, D. G. Revin, S. Y. Zhang, and A. M. Sanchez, Ultramicroscopy **157**, 91 (2015).
[23] D. J. Singh and L. Nordstrom, *Planewaves, Pseudopotentials and the LAPW Method*, 2nd ed. (Springer, New York, 2010).
[24] P. Blaha, K. Schwarz, G. Madsen, D. Kavasnicka, and J. Luitz, *WIEN2k, An Augmented Plane Wave + Local Orbitals Program for Calculating Crystal Properties* (Karlheinz Schwarz, Techn. Universität Wien, Austria, 2001).
[25] C. Loschen, J. Carrasco, K. M. Neyman, and F. Illas, Phys. Rev. B **75**, 035115 (2007).
[26] P. E. Blöchl, O. Jepsen, and O. K. Andersen, Phys. Rev. B **49**, 16223 (1994).
[27] M. Nelhiebel, P.-H. Louf, P. Schattschneider, P. Blaha, K. Schwarz, and B. Jouffrey, Phys. Rev. B **59**, 12807 (1999).
[28] C. Hébert-Souche, P.-H. Louf, P. Blaha, M. Nelhiebel, J. Luitz, P. Schattschneider, K. Schwarz, and B. Jouffrey, Ultramicroscopy **83**, 9 (2000).
[29] H. von Känel, N. Onda, and L. Miglio, in *Science and Technology of Thin Films*, edited by F. C. Matacotta and G. Ottaviani (World Scientific Publishing Co., Singapore, 1995), p. 32.
[30] C. Adamo, X. Ke, H. Q. Wang, H. L. Xin, T. Heeg, M. E. Hawley, W. Zander, J. Schubert, P. Schiffer, D. A. Muller, L. Maritato, and D. G. Schlom, Appl. Phys. Lett. **95**, 112504 (2009).
[31] L. Ranno, A. Llobet, R. Tiron, and E. Favre-Nicolin, Appl. Surf. Sci. **188**, 170 (2002).
[32] T. W. Darling, A. Migliori, E. G. Moshopoulou, S. A. Trugman, J. J. Neumeier, J. L. Sarrao, A. R. Bishop, and J. D. Thompson, Phys. Rev. B **57**, 5093 (1998).
[33] M. Abbate, F. M. F. de Groot, J. C. Fuggle, A. Fujimori, O. Strebel, F. Lopez, M. Domke, G. Kaindl, G. A. Sawatzky, M. Takano, Y. Takeda, H. Eisaki, and S. Uchida, Phys. Rev. B **46**, 4511 (1992).
[34] H. Kurata and C. Colliex, Phys. Rev. B **48**, 2102 (1993).
[35] H. L. Ju, H.-C. Sohn, and K. M. Krishnan, Phys. Rev. Lett. **79**, 3230 (1997).
[36] M. Varela, M. P. Oxley, W. Luo, J. Tao, M. Watanabe, A. R. Lupini, S. T. Pantelides, and S. J. Pennycook, Phys. Rev. B **79**, 085117 (2009).
[37] S. Kobayashi, Y. Tokuda, T. Mizoguchi, N. Shibata, Y. Sato, Y. Ikuhara, and T. Yamamoto, J. Appl. Phys. **108**, 124903 (2010).
[38] T. Riedl, T. Gemming, W. Gruner, J. Acker, and K. Wetzig, Micron **38**, 224 (2007).
[39] S. Zhang, K. J. T. Livi, A.-C. Gaillot, A. T. Stone, and D. R. Veblen, Am. Mineral. **95**, 1741 (2010).
[40] J. C. Slater, Adv. Quant. Chem. **6**, 1 (1972).
[41] J. C. Slater and K. H. Johnson, Phys. Rev. B **5**, 844 (1974).